

Embedded RANS-BEM Tidal Turbine Design

Simon C. McIntosh*, Conor F. Fleming and Richard H.J. Willden

Department of Engineering Science, University of Oxford

Parks Road, Oxford, OX1 3PJ, UK

E-mail: *simon.mcintosh@eng.ox.ac.uk

Abstract—Traditional blade element momentum methods are applied as internal boundary conditions within three-dimensional Reynolds averaged Navier-Stokes simulations (RANS-BEM) forming an expedient method of modelling axial flow turbines operating within constrained flows.

This solution technique is implemented, extended to include the effects of tip-loss on rotor operation and validated against industry standard analytical blade element methods for an unconstrained flow. An excellent agreement between models is shown.

A rotor design-tool based on the targeted achievement of uniform stream-wise thrust loading is developed alongside the RANS-BEM method. This design-tool is then used to generate a series of bespoke ducted and un-ducted rotor designs. A 17 % improvement in power performance is attained for a ducted rotor designed specifically for operation within a duct when compared to a rotor designed for un-ducted operation placed in a duct.

Comparisons are finally made between the embedded blade element method and a number of three-dimensional blade-resolved simulations. Excellent agreement is achieved for tip-speed-ratios in excess of the maximum power point. At lower tip-speed-ratios a divergence in solutions is observed between methods. The discrepancies are attributed to either a stall delay due to span-wise flows or an unforeseen difference in rotor geometries utilised by each solution technique; an as-yet unresolved issue forming the subject of further research.

Index Terms—turbine, design, BEM, RANS, duct

I. INTRODUCTION

Widespread and continued use of one-dimensional analytical Blade Element Momentum methods (henceforth referred to as "analytical-BEM") across both academic and industrial sectors is testament to the value of the technique as an accurate and computationally efficient wind turbine performance prediction tool. Whilst most suited to cases presenting an unbounded uniform inflow, modifications to the baseline analytical method have been made to incorporate a number of secondary flow features such as: moderate vertical velocity shear; tower shadow and unsteady inflows [1]. Unfortunately, as the perturbation size away from a uniform unbounded inflow is increased, assumptions implicit within the model are seen to breakdown and other methods, capable of accurately modelling large departures from the uniform flow condition, are sought.

Tidal rotors designed to operate at very high blockage ratios are frequently proposed as viable methods of exceeding the unbounded Betz limit, often by multiple times [2]. In the case of axial flow rotors, this results in close spaced operation with significant levels of intra-rotor flow coupling [3]. In addition to high levels of flow blockage, flow accelerators such as

ducts are also undergoing commercial development as possible techniques for increasing the energy capture of a particular device [4].

Rotor ducting and flow blockage are known to significantly alter the local flow environment at the rotor plane [5], rendering analytical-BEM approaches less workable. An alternate technique, combining a Reynolds Averaged Navier-Stokes RANS representation of the flow field with a BEM representation of the rotor (henceforth referred to as RANS-BEM) is proposed; similar to that developed in [3].

This model is first validated against an industry standard analytical-BEM model for a rotor operating in an unbounded flow, achieving excellent agreement. Next, a design technique utilising RANS-BEM capable of iteratively adjusting a rotor's geometry to optimise the design of both ducted and un-ducted axial flow rotors in blocked flows is presented. Finally, a comparison of the constrained RANS-BEM model is made with a number of fully blade-resolved RANS simulations.

II. METHODS

In blade element momentum theory, the rotor is modelled as a series of concentric annuli. At each radial station, the axial and swirl induction factors and the angle of attack are calculated. Look-up tables are used to find the corresponding coefficients of lift and drag, in this case provided by wind tunnel experiment. The coefficients, together with blade geometry, twist and taper, are used to compute the resultant blade forces. The procedure is repeated iteratively until the angle of attack, induction factors and blade forces are in balance and a converged solution results.

Embedding a BEM model within a RANS solver is found to be fairly straight forward. An overview of the computational mesh, domain size and pertinent geometrical features of the RANS-BEM and blade-resolved models is given in Section II-A. Following this, Section II-B details the RANS-BEM implementation, including the application of a tip-loss model necessary for the solution of un-ducted flows. The RANS-BEM technique is then advanced via a coupling with an iterative design-tool to enable the design of both ducted and un-ducted tidal axial flow rotors, Section II-C.

A. Computational Set-up

The following investigations concern the performance prediction and design of ducted and un-ducted tidal rotors. The

following solution techniques are used: analytical-BEM, three-dimensional embedded RANS-BEM and three-dimensional fully blade-resolved RANS simulations.

A base-line three-bladed model scale rotor [6] employing a Goettingen 804 aerofoil section is simulated in all three cases. Force coefficient data for the profile operating at a Reynolds number of 30,000 [7] is used to account for the rotor blades in the case of the analytical-BEM and RANS-BEM whilst a full geometric reconstruction of the Goettingen 804 profile is employed in the blade-resolved simulations. All solutions using the analytical-BEM method represent unbounded flows. Blockage and the effects of duct geometry are explicitly resolved for the RANS-BEM and blade-resolved simulations by inclusion of the pertinent geometrical features within the computational mesh as either symmetry or non-slip boundaries. Flow blockage effects are simulated by placing the rotor in a 1.5 m wide by 1 m deep channel, with symmetry boundaries placed at 0.75 m either side and 0.6 m and 0.4 m above and below the rotor centreline. We choose to maintain a constant outer device diameter of 0.309 m. Simulation in this manner presents a consistent flow blockage of 5% between ducted and un-ducted designs. The use of lateral symmetry conditions simulates a fence of tidal turbines with a centre-to-centre spacing of 4.85 rotor diameters. A rigid lid approximation is used in place of a free-surface. This is considered to be a valid approximation to free-surfaces flows for the flow blockage ratio being considered [8].

Both ducted and un-ducted rotors are constrained to have a maximum outer dimension of 0.309 m. For un-ducted operation this represents the rotor diameter R . For ducted operation this maximum dimension represents the outer duct diameter, with the rotor geometry down-scaled to fit the inner duct dimension. Figure 1 presents illustrative examples of the computational meshes used for the RANS-BEM and blade-resolved ducted simulations. The duct geometry used within this study is taken from a parallel piece of work detailing the parametric design of bi-directional tidal turbine ducts using idealised porous disk actuators [9]. A geometrical description of the best performing design (duct H, reproduced here in Fig. 2) is taken from this study and is used as a starting point for the following ducted rotor case studies. The computational meshes presented here produce grid resolved solutions for each simulation technique [9]. Overall cell counts for each domain are summarised below in table I. As shown, the representation

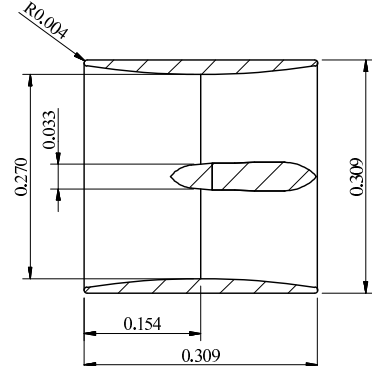


Fig. 2. Duct H geometry [9]. All dimensions in meters.

solution techniques, further reducing computational cost below the cost of unsteady blade-resolved simulations. A summary of approximate solution times for each method is given in Section III-C, Table III.

B. Embedded RANS-BEM

The blade element momentum method is implemented as a boundary condition within a FLUENT [10] simulation, with the rotor represented as a thin disk. As BEM does not account for discrete blades, the forces at each radial station are averaged circumferentially, permitting the steady (time-averaged) solution of rotor flows. The axial and tangential forces imparted by the rotor on the flow can be reproduced via the respective application of a jump in static pressure Δp across the disk

$$\Delta p = \frac{1}{2} \rho U^2 \sigma(r) (C_l \cos \phi + C_d \sin \phi), \quad (1)$$

and the specification of a swirl velocity u_θ down-stream of the disk

$$u_\theta = -\frac{\frac{1}{2} \rho U^2 \sigma(r) (C_l \sin \phi - C_d \cos \phi)}{\Delta p u_x}. \quad (2)$$

C_l and C_d are the sectional lift and drag coefficients. ϕ is taken as the angle between the resultant blade-incident velocity vector and the rotor plane. The local solidity $\sigma(r)$ based on local chord c and local radius r defined as

$$\sigma(r) = \frac{Nc}{2\pi r}. \quad (3)$$

The chord-wise velocity component U defined as the resultant of the stream-wise u_x and tangential $\frac{u_\theta}{2}$ components

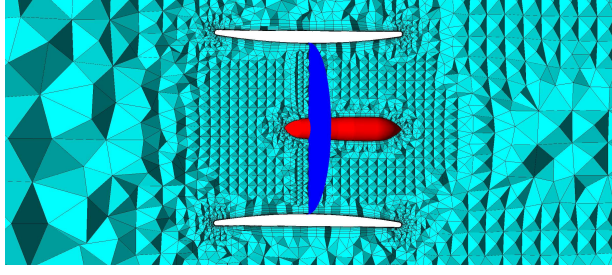
$$U = \sqrt{\frac{u_\theta^2}{4} + u_x^2}. \quad (4)$$

Where, consistent with many analytical-BEM models, the swirl component evaluated at the disk plane is assumed to reach half its downstream value (Eq. 2). Unlike the equal division of stream-wise momentum loss, the physical mechanisms responsible for a 50-50 split in swirl development up- and down-stream of the rotor plane are less clear. This heuristic choice is therefore taken in the first place to aid comparison with industry standard analytical-BEM models. The influence

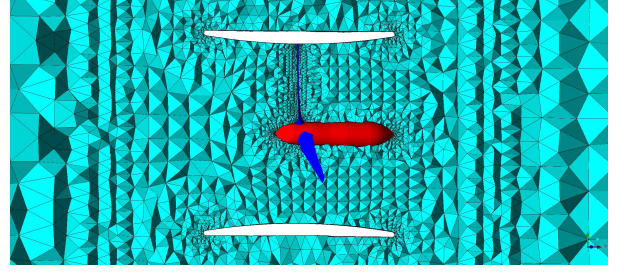
TABLE I
RANS-BEM VS. BLADE-RESOLVED: THE INFLUENCE OF SOLUTION METHOD ON GRID RESOLVED CELL COUNT.

Computational Domain	Cell Count
RANS-BEM	700,000
Blade-resolved	4,400,000

of the rotor as a thin boundary leads to a significant reduction in overall cell-count (~ 6 times) representing a considerable saving in computational cost. In addition to this, the implementation of the RANS-BEM model permit the use of steady



(a) RANS-BEM.



(b) Blade-resolved.

Fig. 1. An illustrative comparison of RANS-BEM and Blade-resolved computational meshes highlighting relative mesh density along a common center plane.

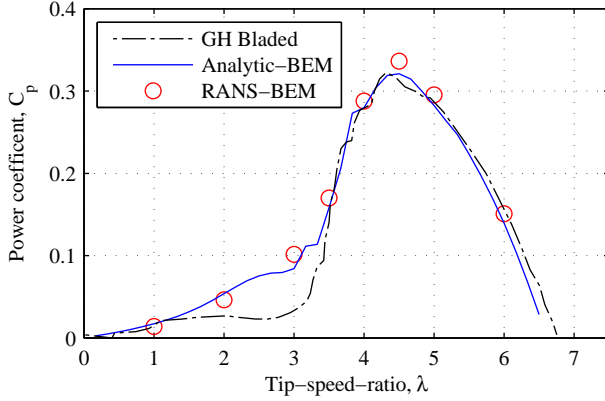


Fig. 3. Comparison of RANS-BEM embedded within FLUENT, Garrad Hassan BLADED (GH), and an in-house analytical-BEM solution (UoO)

of helical vortex wakes originating close to the tips of unducted rotors is accounted for here via the application of Prandtl's tip-loss model [11] in the form of a tip-loss factor F

$$F = \frac{2}{\pi} \arccos \exp \frac{N(1 - \frac{R}{r})}{2 \sin \phi \pi}, \quad (5)$$

to the blade local stream-wise velocity component u_x . It has been shown that this tip-loss mechanism is not present in ducted rotor flows [9]. In this case the tip-loss model is disabled by setting the loss factor equal to unity for all radial stations.

In order to verify the embedded BEM method against analytical-BEM, an effectively unbounded rotor (1% blockage) is simulated. To replicate the analytical-BEM solution, where no flow is modelled inboard of the first radial annulus, the computational model is constructed to include a cylindrical slip wall boundary inside the first radial station. This cylindrical inner boundary extends from the inlet to the outlet of the domain directly replicating the solution space modelled using the analytical-BEM method. Figure 3 illustrates a good agreement between BEM embedded within a steady FLUENT simulation (RANS-BEM) and the analytical-BEM solution. At low tip-speed-ratios, disagreement is visible between in-house analytical-BEM / RANS-BEM and results achieved using GH

Bladed [12]. These inconsistencies are likely due to variations in aerofoil input data in the post stall region and hence the specific choice of post-stall model used by each technique. Good agreement is maintained between in-house analytical-BEM and the RANS-BEM model, both of which employ a widely accepted post-stall model by Viterna and Corrigan [13].

C. Embedded RANS Blade Element Method Design Tool

The design method presented here extends the capabilities of the standard RANS-BEM prediction method detailed in Section II-B to allow the iterative design of a tidal rotor operating in-situ. The design method is centred on the idea of achieving a constant target local thrust coefficient across the disk,

$$c_x = \frac{\delta F_x}{\frac{1}{2} \rho \delta A u_x^2}, \quad (6)$$

at a blade angle of attack consistent with the maximum blade lift to drag ratio and for a rotor operating at a user specified tip-speed-ratio. δF_x is the stream-wise load imparted on an elemental disk element of area δA . Once initiated, the design method iteratively adjusts blade chord, to influence local stream-wise loading, and blade twist, to modify the local angle of attack, whilst the solution progresses. Lanchester [14] and Betz [15] show that, for an unbounded rotor, optimal power performance is coincident with a stream-wise rotor thrust F_x yielding a coefficient of

$$C_x = \frac{F_x}{\frac{1}{2} \rho A U_\infty^2} = \frac{8}{9} \quad (7)$$

resulting in an optimum target local thrust coefficient of $c_x = 2$, as defined in Eq. 6. Noting that optimal performance occurs at $u_x = \frac{2U_\infty}{3}$.

For solutions containing multi-body viscous interactions, e.g. a rotor in a duct, the evaluation of optimum local disk loading is far less straightforward. In such cases the optimum power may not occur at a local $c_x = 2$ and an iterative solution maximising C_p is instead employed. First, turbine designs for a number of coarsely spaced local disk loadings are made, creating a simple one-dimensional design space, as shown in Fig. 4. A cubic interpolant is then fit through the initial trials to better estimate the optimum stream-wise loading. This estimate, $c_x = 1.1$ for the ducted case shown in Fig. 4, is then

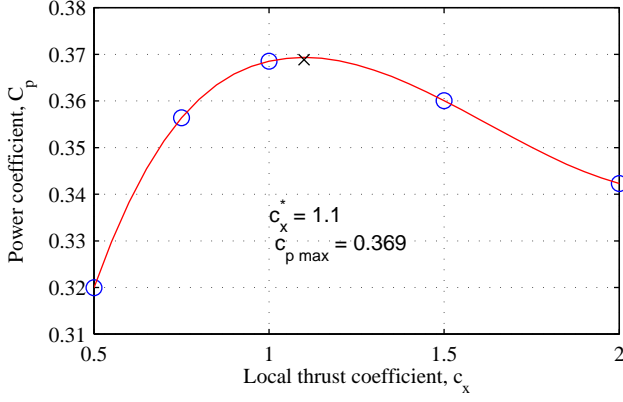


Fig. 4. Illustration of the dependence of rotor performance on local thrust coefficient. Blue circles - initial trials; red line - cubic interpolant; black cross - final design.

run through the design tool once more producing an optimal power coefficient, based on outer duct area, of $C_p = 0.37$.

Situations can arise, especially close to the rotor hub, where iterations towards a high target axial loading lead to significant blade overlap, indicated here by local solidity exceeding unity

$$\sigma(r) = \frac{Nc}{2\pi r} > 1. \quad (8)$$

For these cases once a present upper limit on local solidity is reached, further increases in local thrust coefficient is achieved by incrementally increasing the target local blade angle of attack from the optimum lift-to-drag value α_{LD} up to a value α_{max} corresponding to either the maximum achievable local blade circumferential force coefficient

$$c_{\tau blade} = C_l \sin \phi - C_d \cos \phi, \quad (9)$$

or the incidence at which the maximum achievable local blade thrust coefficient occurs

$$c_{x blade} = C_l \cos \phi + C_d \sin \phi. \quad (10)$$

We define α_{max} as the angle of attack at which the first maximum occurs. An illustrative example of this target angle of attack selection strategy is given in Fig. 5 for the Goettingen 804 aerofoil section. Solidity and angle of attack limits are set to $\sigma = 1.25$ (accommodating slight blade overlap close to the hub) and $\alpha = \alpha_{max}$ respectively. Once these limits are met, axial loading can no longer be increased. This results in an underachievement in axial thrust for the radial sections in question.

III. RESULTS

The influence of both flow blockage and rotor ducting on rotor performance is now presented, with comparisons made to an analytical unbounded BEM solution employing a generic base-line rotor design.

It is expected that a rotor designed specifically for an altered flow environment within a duct would out-perform a rotor that has been specifically designed for un-ducted operation. To

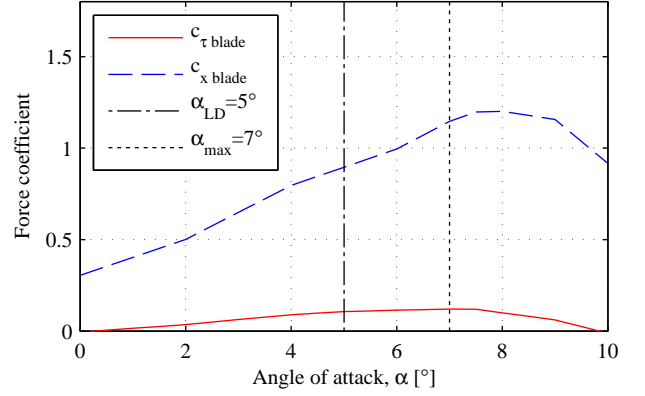


Fig. 5. An illustrative example of acceptable target blade angle of attacks ranging from optimum lift-to-drag to the first maximum in either torque or thrust coefficient for a solidity limited radial section (Goe804, Re 30,000,).

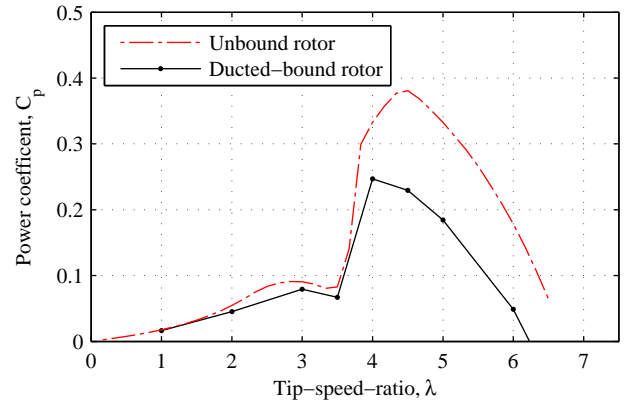


Fig. 6. Illustration of the effects of blockage and ducting on rotor power performance prediction (analytical-BEM / RANS-BEM).

test this hypothesis, the aforementioned iterative rotor design-tool is implemented within the RANS-BEM model, generating bespoke rotor designs for ducted and un-ducted flow-fields.

The design-tool is first tested for an un-ducted rotor operating within a blocked flow, with the methods effectiveness rated by comparison of the performance of the bespoke rotor against the base-line rotor. A bespoke rotor design is then pursued for a ducted case. Finally, the rotor designed for un-ducted operation is placed within a duct to quantify the importance of including the influence of ducting in the evolution of a ducted rotor design.

A. Departures From Unbounded Flow

A comparison between the unbounded analytical-BEM and RANS-BEM methods is now made to better illustrate the influence of blockage and ducting on rotor performance. In Fig. 6 we present an unbounded un-ducted result for the analytical-BEM case as the analytical-BEM method used is not capable of incorporating the effects of blockage and ducting.

Using the same rotor we also present a RANS-BEM solution

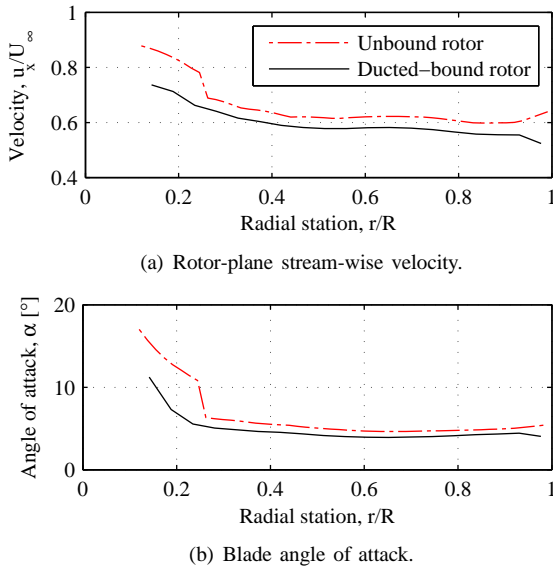


Fig. 7. Illustration of the effects of blockage and ducting on rotor flow-field (analytical-BEM / RANS-BEM, $\lambda = 4.5$).

for a blocked ducted flow¹. Rather than an isolated study into either the effects of blockage or ducting, the results presented here aim to portray significant differences arising in the prediction of rotor performance using each technique; hence justifying the requirement for a design method capable of encapsulating significant additional flow features that occur within tidal flows. The rotor power curves, shown in Fig. 6 illustrate distinctly different performance predictions both in terms of overall shape and value. Application of blockage and ducting leads to a decrease in maximum predicted power of $\sim 23\%$ along with a slight widening of the power curve and the movement of the maximum power point to a lower tip-speed-ratio.

The large differences in the integral rotor performance coefficients shown in Fig. 6 are indicators of significant differences in the blade local flow environment predicted by each technique. Figure 7 illustrates the effect of blockage and ducting on the blade local axial flow velocity for a rotor operating at a tip-speed-ratio of $\lambda = 4.5$. Here, the combined effect of blockage and ducting is shown to reduce the axial flow velocity by $\sim 10\%$. This leads to a delay in blade stall on the inboard radial sections for the ducted solution, leading to the shift in maximum C_p to a lower tip-speed-ratio, as shown in Fig. 6. Blade stall inboard of the $\sim 25\%$ r/R radial station in the analytical-BEM simulation results in higher flow rates through the center of the turbine, almost recovering free-stream velocities close to the hub. Towards the outer radial stations a reduction in axial flow velocity for the RANS-BEM case is shown; attributed to the interaction of the rotor tips with boundary layers growing on the inner surface of the

¹To aid comparison between the analytic and RANS-BEM methods, both solutions undertaken here are solved without the use of a tip-loss model. Typically un-ducted simulations would employ such a model whilst ducted solutions would not [9].

duct. An increase in velocity is shown for the analytical-BEM case which is attributed to the absence of a tip-loss model². This permits higher axial velocities than would be seen under normal operating conditions for the baseline rotor.

In summary, it is shown that strong fluid-dynamic interactions, such as the blocked / ducted case studied here, are responsible for large departures from the unbounded uniform inflow results generated by analytical-BEM techniques. Embedding a BEM solution within a RANS solver is potentially capable of addressing these interactions whilst retaining the advantages of a computationally light solution. This claim is later verified in Section III-C, where good agreement is achieved between results of RANS-BEM and blade-resolved simulations³.

B. RANS-BEM Rotor Designs

A number of design cases are now presented to illustrate the capabilities of the RANS-BEM design tool. The rotors tested, listed in Table II, comprise the baseline rotor along with RANS-BEM designs for un-ducted and ducted operation. Firstly, an alternate design to the baseline rotor (rotor I) is

TABLE II
A SUMMARY OF ROTOR DESIGN DESIGNATIONS.

Label	Description
Rotor I	Baseline rotor
Rotor II	Rotor designed for un-ducted operation in a blocked flow using RANS-BEM design tool
Rotor III	Rotor designed for operation within duct H in a blocked flow using RANS-BEM design tool

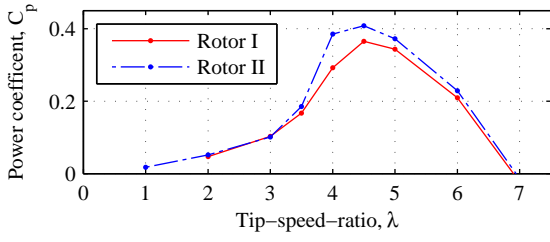
made for a rotor operating in a blocked (5 % by area) but un-ducted configuration (rotor II). Next, a design for a blocked (5 %) rotor operating within duct H is presented (rotor III). Finally all rotors are compared for operation within duct H. These case studies illustrate the advantages of a fully coupled (embedded) tidal turbine design tool.

Figure 8(a) illustrates a comparison between the power performance of rotors I and II operating in an un-ducted configuration in a blocked flow. Whilst the overall shape of the power coefficient curves remain the same between the two rotors, rotor II displays an appreciable increase in maximum power coefficient of $\sim 12\%$. Figure 8(b) illustrates the corresponding comparison of overall thrust coefficient. Whilst the overall shapes are again similar, a higher thrust value for rotor II results.

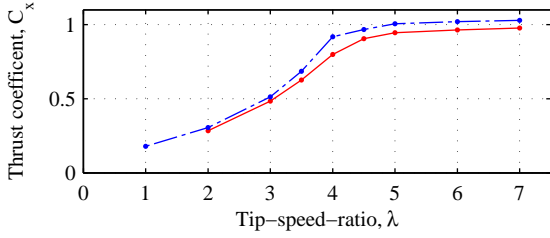
Figure 9(a) illustrates the comparison of rotor power performance for the baseline rotor (I) operating in duct H and a design-tool generated rotor (III). An increase in maximum power coefficient of $\sim 14\%$ over the baseline design is achieved. This increase is accompanied by a reduction in overall rotor thrust coefficient, indicating an increase in the efficiency of energy extraction (Fig. 9(b)). A sharp decrease in power coefficient is shown in Fig. 9(a) at low tip-speed-ratios. The absence of a helical vortex wake, modelled here by

²The tip-loss model is disabled for all ducted flow simulations [9]

³For the case of the RANS-computed input aerofoil polar.

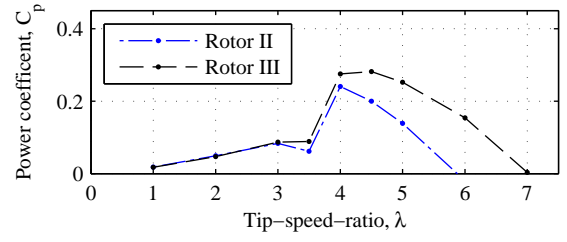


(a) Power Performance.

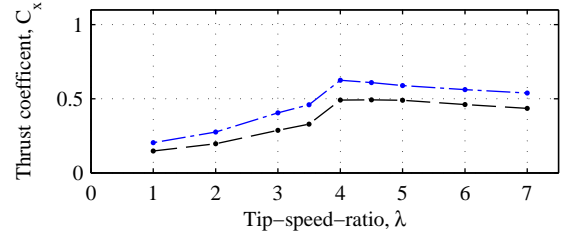


(b) Thrust Performance.

Fig. 8. An illustrative comparison of rotor performance for rotors I and II (un-ducted) in 5 % blockage.

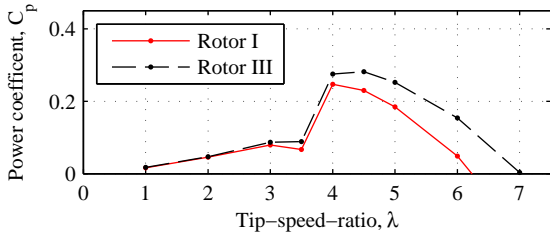


(a) Power Performance.

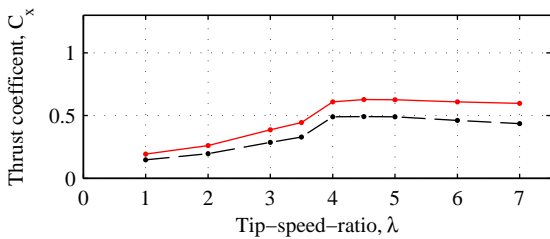


(b) Thrust Performance.

Fig. 10. An illustrative comparison of rotor performance for rotors II and III in duct H, 5 % blockage.



(a) Power Performance.



(b) Thrust Performance.

Fig. 9. An illustrative comparison of rotor performance for rotors I and III in duct H, 5 % blockage.

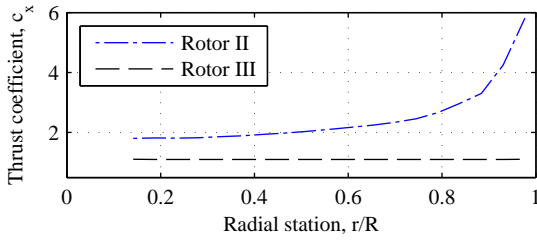
disabling the tip-loss model, results in an increase in stream-wise flow speeds across the outer blade stations. This in turn results in higher blade local angles of attack being maintained across the outer radial stations. As tip-speed-ratio is reduced, the more benign blade stall associated with a helical vortex wake is replaced by a more abrupt rotor stall across the outer blade stations, leading to a sharp drop in power.

Increases in maximum power coefficient of 12% and 14% are achieved by rotors II and III, with reference to rotor I, for un-ducted and ducted operation respectively.

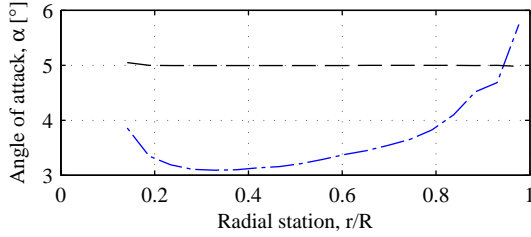
In order to isolate the influence of the baseline rotor geometry (rotor I) from that of the embedded RANS-BEM design tool, a comparison is now made between rotors II

and III operating within duct H. Figure 10(a) illustrates a substantial increase in power coefficient of $\sim 17\%$ for rotor III over II, showing both the effectiveness of the embedded design-tool and the importance of flow-field interactions for tidal turbine design. Once again, Fig. 10(b) illustrates a lower overall rotor thrust coefficient for the superior performing device, and hence a greater overall energy extraction efficiency, generated by the rotor designed for purpose (operation within duct H). Examination of local disk loading and angle of attack in Figs. 11(a) and 11(b) for the two designs operating at a tip-speed-ratio of $\lambda = 4.5$ illustrates the influence of duct H on rotor operation. Whilst the rotor designed for a uniform disk loading (rotor III) achieves the optimal target thrust, the rotor designed for un-ducted operation (rotor II) displays a far greater local stream-wise loading increasing to a value approaching $c_x = 6$ close to the tips (likely to be a combination of the absence of a tip loss model for ducted flows and local flow acceleration due to the influence of the duct itself). Figure 11(b) shows the achievement of the target blade local angle of attack for all radial stations of $\alpha = \alpha_{LD} = 5^\circ$ by the rotor designed for ducted flow (a requirement for optimal blade aerodynamic efficiency). The rotor designed for un-ducted flow (rotor II) shows a variable blade local angle of attack resulting in far greater blade aerodynamic losses, a contributing factor to the poorer power performance and associated higher overall stream-wise thrust coefficient observed for rotor II in duct H.

This section concludes with a geometric comparison of rotors II and III. Blade twist is shown in Fig. 12(a) to be greater for the rotor designed for ducted operation. Differences in blade twist are seen to increase towards the tips. Here, rotor II, designed to accommodate the detrimental effects of tip loss, exhibits tip wash-out, which is absent in the rotor III design. Figure 12(b) shows a comparison of local solidity for the two

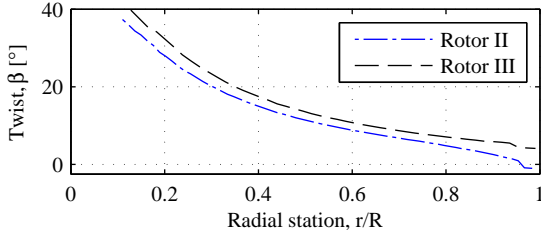


(a) Blade local thrust coefficient, c_x .

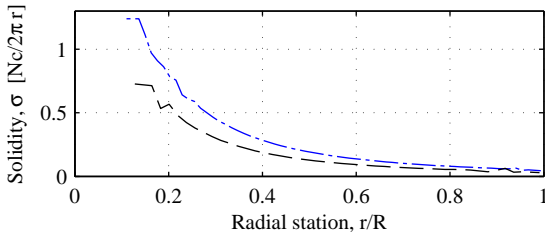


(b) Blade local angle of attack, α .

Fig. 11. An illustrative comparison between rotors II and III operating in duct H, highlighting elements of the blade local flow condition ($\lambda = 4.5$).



(a) Blade twist, β .



(b) Blade solidity, σ .

Fig. 12. A geometrical comparison of rotors II and III.

rotor designs. Here, rotor III displays a much lower solidity than rotor II. As with blade twist, this difference is shown to be a strong function of radial station.

The development and use of the embedded RANS-BEM design-tool has illustrated the importance of the inclusion of the combined effects of both blockage and ducting within any tidal turbine performance prediction method. Strong flow-field couplings should be considered primary drivers for tidal turbine designs and cannot be dismissed as secondary features.

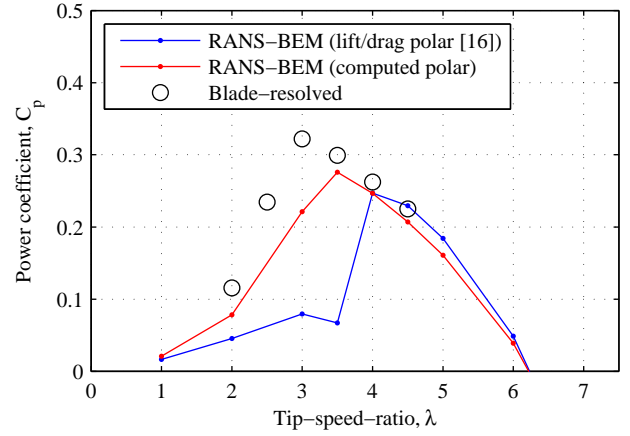


Fig. 13. A comparative example of rotor performance prediction utilising RANS-BEM and blade-resolved solution methods.

C. Blade-resolved Simulation

A series of three-dimensional blade-resolved simulations of a ducted tidal turbine (rotor I in duct H) are now presented with comparison to the RANS-BEM results. Table III presents a comparison of computational cost, in terms of cpu time per tip-speed-ratio, for the RANS-BEM analysis and design tool and the blade-resolved simulations. A significant computational

TABLE III
A COMPARISON OF RELATIVE COMPUTATIONAL COST BETWEEN SOLUTION METHODS.

Method	cpu time per tip-speed-ratio [hours]
RANS-BEM (analysis)	8
RANS-BEM (design-tool)	8
Blade-resolved (analysis)	2000

saving of ~ 250 times is achieved through the use of the RANS-BEM analysis method as opposed to the blade-resolved solutions. Computational cost for a bespoke rotor design operating at a pre-determined tip-speed-ratio and stream-wise thrust is shown to be similar to the cost of a RANS-BEM analysis alone. This is a direct result of the iterative design method employed and is considered to be a valuable attribute of the developed rotor design-tool.

RANS-BEM rotor performance predictions are shown in Fig. 13 for two distinct sets of aerofoil input data. The first set is taken from wind tunnel experiments [16] with the second produced by three-dimensional RANS computation of a Goettingen 804 aerofoil section [9]. Excellent agreement for power performance is observed between RANS-BEM (computed polars) and blade-resolved simulations for tip-speed-ratios greater than $\lambda = 3.5$. Below this value divergence between the two methods is visible, with the blade-resolved results indicating a higher power output than the RANS-BEM method. At a tip-speed-ratio of $\lambda = 3.5$ significant blade stall is predicted by the RANS-BEM technique whilst the blade-resolved sections remain largely attached; the blade resolved model achieves a peak power coefficient of $C_p = 0.32$ at a

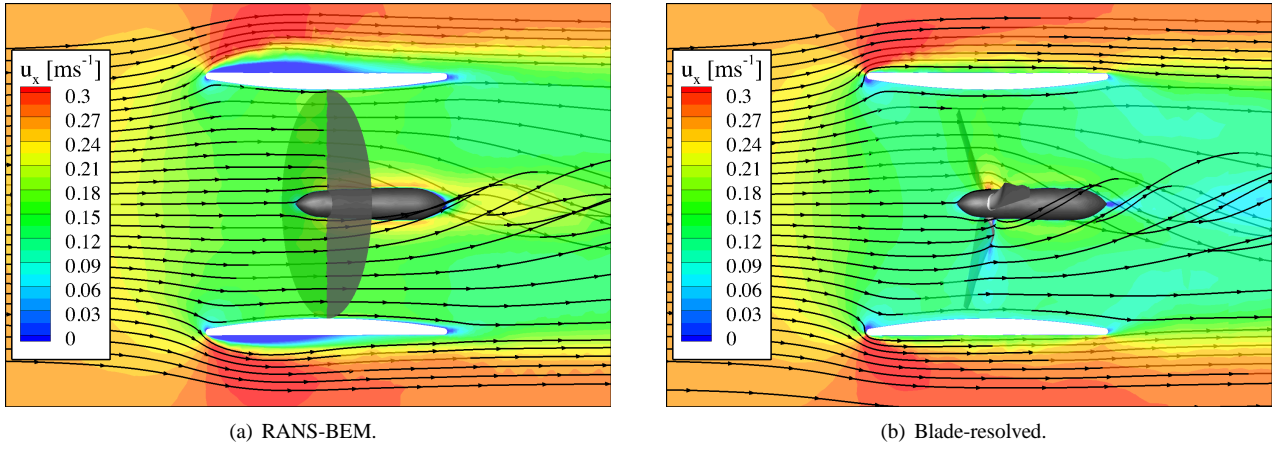


Fig. 14. A comparison between RANS-BEM and blade-resolved ducted rotor flow fields illustrating centreplane stream-wise velocity contours with instantaneous streamlines ($\lambda = 3.5$).

tip-speed-ratio of $\lambda = 3$, at which the RANS-BEM model is significantly stalled. The generating mechanism for this observed difference in power coefficient near peak C_p is not yet fully understood. One possible explanation could be the influence of span-wise flows delaying stall onset to higher blade angles of attack [17]–[19] which is not accounted for within the RANS-BEM model. Whilst an alternative could lie in minor geometrical differences between the rotor geometries employed in the two models; the RANS-BEM rotor is an idealisation of the blade-resolved model which is taken from a CAD drawing of a rotor manufactured for experimental testing, the blades of which are thickened at inboard sections near the hub to improve structural integrity. Agreement between the models is improved at the lowest tip-speed-ratio computed ($\lambda = 2$). A detailed comparison between the RANS-BEM and blade-resolved flow fields is given in Fig. 14. Both flow fields demonstrate broadly similar features with comparable velocity fields including accelerations external to the duct and significant rotation in the turbine’s wake. Differences occur close to the hub, where the RANS-BEM solutions exhibit regions of accelerated flow, and external to the duct, where flow separation evident in the RANS-BEM flow-field is not present in the blade-resolved simulation. These two flow-field inconsistencies are compatible with the arguments given above concerning the geometrical similarity between models close to the hub and the influence of span-wise flows on stall-delay. Further work is required in order to identify the influence of these two mechanisms on the inconsistencies in rotor performance prediction (Fig. 13).

RANS-BEM solutions employing the experimental aerofoil polar show a far larger disagreement with the blade-resolved simulations for tip-speed-ratios below $\lambda < 4$. The source of this difference is likely to be inaccuracies in the RANS computed lift/drag polars at low Reynolds numbers.

IV. CONCLUSIONS

A computationally expedient method of rotor modelling, involving a combination of the widely-used BEM method

and a commercial RANS flow solver, has been developed and validated. A power curve is produced for validation against both industry standard and in-house analytical-BEM tools achieving excellent agreement. The computational cost of blade-resolved simulations is shown to be approximately two orders of magnitude greater than that of BEM-RANS simulations.

A method is developed that enables rotor design for a given flow environment. Comparisons are made between the performances of ducted devices with generic and bespoke rotor designs. A 17% increase in maximum power coefficient is achieved for a rotor designed for ducted operation opposed to a rotor designed for un-ducted operation, operating in a duct.

A series of blade-resolved simulations of the ducted device are carried out. Excellent agreement is achieved between blade-resolved simulation and RANS-BEM simulations employing computed polars for tip-speed-ratios beyond the maximum power point. At lower tip-speed-ratios a divergence between the RANS-BEM results (computational polar) and the blade-resolved simulations is shown. It is believed that either a delayed stall onset due to span-wise flows or geometrical inconsistencies between models is responsible for differences in the model predictions.

Errors arising from the limited ability of RANS solvers to accurately predict lift and drag coefficients for an aerofoil operating at low Reynolds numbers are identified. The RANS-BEM method employing experimental aerofoil polars is presented as the solution method in which most confidence is placed.

V. ACKNOWLEDGMENTS

This study was completed as part of the PerAWaT project commissioned by the Energy Technologies Institute (ETI).

REFERENCES

- [1] M. O. L. Hansan, *Aerodynamics of Wind Turbines*. James & James Ltd., 2008.
- [2] J. I. Whelan, J. M. R. Graham, and J. Peiró, “A free-surface and blockage correction for tidal turbines,” in *Journal of Fluid Mechanics*, vol. 624, 2009, pp. 281–291.

- [3] M. E. Harrison, W. M. J. Batten, and A. S. Bahaj, "A blade element actuator disc approach applied to tidal stream turbines," in *OCEANS 2010*, sept. 2010, pp. 1–8.
- [4] OpenHydro LTD. (2011). [Online]. Available: www.openhydro.com
- [5] C. S. K. Belloni and R. H. J. Willden, "Flow field and performance analysis of bidirectional and open-centre ducted tidal turbines," in *9th European Wave and Tidal Energy Conference*, 2011.
- [6] J. I. Whelan and T. Stallard, "Arguments for modifying the geometry of a scale model rotor," in *9th European Wave and Tidal Energy Conference*, 2011.
- [7] U. Hassan, "A wind tunnel investigation of the wake structure within small wind turbine farms," Garrad Hassan and Partners Ltd., Tech. Rep. ETSU WN 5113, 1993.
- [8] C. A. Consul, R. H. J. Willden, and S. C. McIntosh, "An investigation of the influence of free surface effects on the hydrodynamic performance of marine cross-flow turbines," in *9th European Wave and Tidal Energy Conference*, 2011.
- [9] F. Fleming, S. C. McIntosh, and R. H. J. Willden, "Design and analysis of a bi-directional ducted tidal turbine," in *9th European Wave and Tidal Energy Conference*, 2011.
- [10] "Ansys fluent 12.0 user's guide."
- [11] L. Prandtl and A. Betz, "Vier abhandlungen zur hydrodynamik und aerodynamic," Göttingen, Tech. Rep., 1927.
- [12] E. A. Bossanyi, "GH Bladed - Theory Manual," Garrad Hassan and Partners Ltd., Tech. Rep. 282/BR/009, 2003.
- [13] L. A. Viterna and R. D. Corrigan, "Fixed pitch rotor performance of large horizontal axis wind turbines," in *DOE/NASA Workshop on Large Horizontal Axis Wind Turbines, Cleveland, Ohio, USA*, 1981, pp. 69–85.
- [14] F. W. Lanchester, "A contribution to the theory of propulsion and the screw propeller," in *Transactions of the Institution of Naval Architects*, vol. 57, 1915, pp. 98–116.
- [15] A. Betz, "Das maximum der theoretisch möglichen ausnützung des windes durch windmotoren," in *Zeitschrift für das gesamte Turbinenwesen*, vol. 26, 1920, pp. 307–309.
- [16] S. J. Miley, "A catalog of low reynolds number airfoil data for wind turbine applications," Texas A&M University, Tech. Rep. DE82-021712.NTIS, 1982.
- [17] D. H. Franklin, "Preliminary study of radial flow effects on rotor blades," in *Journal of the American Helicopter Society*, vol. 11, 1966, pp. 1–21.
- [18] B. W. McCormick, *Aerodynamics Aeronautics and Flight Mechanics*. Wiley, 1995.
- [19] C. A. Crawford, "Advanced engineering models for wind turbines with application to the design of a coning rotor concept," Ph.D. dissertation, University of Cambridge, 2006.